The Astrophysical Journal, 717:250–256, 2010 July 1 doi:10.1088/0004-637X/717/1/250
© 2010. The American Astronomical Society. All rights reserved. Printed in the U.S.A.

THE SUB-ARCSECOND HARD X-RAY STRUCTURE OF LOOP FOOTPOINTS IN A SOLAR FLARE

E. P. Kontar, I. G. Hannah, N. L. S. Jeffrey, and M. Battaglia
Department of Physics and Astronomy, University of Glasgow, G12 8QQ, UK
Received 2009 November 12; accepted 2010 May 3; published 2010 June 10

ABSTRACT

The newly developed X-ray visibility forward fitting technique is applied to the *RHESSI* data of a limb flare to investigate the energy and height dependence on sizes, shapes, and position of hard X-ray (HXR) chromospheric footpoint sources. This provides information about the electron transport and chromospheric density structure. The spatial distribution of two footpoint X-ray sources is analyzed using PIXON, Maximum Entropy Method, CLEAN, and visibility forward fit algorithms at nonthermal energies from ∼20 to ∼200 keV. We report, for the first time, the vertical extents and widths of HXR chromospheric sources measured as a function of energy for a limb event. Our observations suggest that both the vertical and horizontal sizes of footpoints are decreasing with energy. Higher energy emission originates progressively deeper in the chromosphere, consistent with downward flare accelerated streaming electrons. The ellipticity of the footpoints grows with energy from ∼0.5 at ∼20 keV to ∼0.9 at ∼150 keV. The positions of X-ray emission are in agreement with an exponential density profile of scale height ∼150 km. The characteristic size of the HXR footpoint source along the limb decreases with energy, suggesting a converging magnetic field in the footpoint. The vertical sizes of X-ray sources are inconsistent with simple collisional transport in a single density scale height but can be explained using a multi-threaded density structure in the chromosphere.

Key words: Sun: activity – Sun: flares – Sun: particle emission – Sun: X-rays, gamma rays

Online-only material: color figures

1. INTRODUCTION

In the standard flare scenario, electrons are accelerated in the coronal stream downward toward the dense layers of the solar atmosphere, where they are stopped via collisions producing intense hard X-ray (HXR) emission in the chromosphere. Higher energy electrons penetrate deeper into the chromosphere. Therefore, measurements of the spatial structure of the HXR emission as a function of energy provide information about the chromospheric density. Being optically thin, X-rays give the most direct information about the spatial and energy distribution of energetic electrons in the solar atmosphere. Prior to the launch of the *Ramaty High Energy Solar Spectroscopic Imager* (*RHESSI*; Lin et al. 2002), HXR instruments typically had limited imaging-spectroscopy capabilities (Kosugi et al. 1992). *RHESSI*'s aptitude to image in various energy ranges opens new horizons for studying the detailed structure of HXR emitting sources in the chromosphere.

RHESSI does not directly image the Sun but uses nine pairs of Rotating Modulation Collimators (RMCs) to time-modulate spatial information in the signal obtained in its germanium detectors (Hurford et al. 2002). Each RMC has a different thickness of its slits and slats, making each sensitive to different spatial scales, providing modulation at nine spatial frequencies. The reconstruction of an image from these time-modulated light curves, can be accomplished by various imaging algorithms (Emslie et al. 2003; Battaglia & Benz 2007; Krucker & Lin 2008; Saint-Hilaire et al. 2008; Dennis & Pernak 2009). The new visibility-based approach to *RHESSI* imaging starts by summing (stacking) the light curves per roll bin over a few spin periods of the spacecraft (Schmahl et al. 2007). The fitted amplitudes and the phases in the individual roll bins are X-ray visibilities. This effectively provides two-dimensional spatial Fourier components (X-ray visibilities) over a wide range of energies (Hurford et al. 2002; Schmahl et al. 2007). To convert the time-modulated signal or X-ray visibilities to an image is an inverse problem (e.g., Piana et al. 2007; Prato et al. 2009). The reconstructed images face unavoidable difficulties due to measurement errors, finite coverage in Fourier space, and the fact that the reconstruction problem is ill-posed. The resulting reconstruction errors and small dynamic range make it difficult to accurately measure source sizes from reconstructed images. At best the imaging resolution is down to 2″, but in practice it is around 7″ for the typical flare nonthermal energy range.

However, the moments of X-ray source distribution (source position, source size, etc.) can be inferred with higher precision either from the time-modulated signal (Aschwanden et al. 2002; Krucker & Lin 2008; Saint-Hilaire et al. 2008; Fivian et al. 2009) or visibilities (Xu et al. 2008; Kontar et al. 2008; Dennis & Pernak 2009; Prato et al. 2009). Thus, *RHESSI* measurements of X-ray source positions can recover sub-arcsecond information using *RHESSI*-modulated light curves (Aschwanden et al. 2002; Liu et al. 2006; Mrozek 2006) or visibilities (Kontar et al. 2008; Dennis & Pernak 2009; Prato et al. 2009). This has allowed clear demonstration of the height–energy dependence of HXR sources—higher energy sources originate at lower heights (Aschwanden et al. 2002; Brown et al. 2002; Liu et al. 2006). This has substantially improved upon previous results with *Yohkoh*/HXT (Matsushita et al. 1992). The recently developed visibility-based technique (Schmahl et al. 2007) allowed Kontar et al. (2008) to improve previous measurements and infer characteristic sizes (FWHM) of HXR footpoints and not just the centroid height. From this, the convergence of the magnetic flux and neutral hydrogen density distribution in the chromosphere was inferred.

In this paper, we study the structure of solar flare HXR sources using various imaging algorithms: PIXON, MEM, CLEAN, and visibility forward fit. Using *RHESSI* X-ray visibilities, we find the characteristic shapes and positions for different energy ranges. We show that the technique of forward fitting X-ray visibilities allows us to determine not only the FWHM of the sources but vertical and horizontal sizes of the sources,

which are required for examining the density structures of the chromosphere. Theoretical relationships were compared with observations to find the density structure of the chromosphere. The vertical sizes of the X-ray sources are found to be larger than the ones predicted by a hydrostatic atmosphere in thick-target scenario. However, assuming that the electrons are propagating along several narrow threads with different density profiles can explain the measured vertical sizes of the sources.

2. X-RAY VISIBILITIES AND CHARACTERISTIC SIZES

The spatial information about an X-ray source measured by *RHESSI* for a given energy range and time interval can be presented (Hurford et al. 2002; Schmahl et al. 2007) as two-dimensional Fourier components or X-ray visibilities:

$$V(u, v; \epsilon) = \int_x \int_y I(x, y; \epsilon) e^{2\pi i(xu+yv)} dx dy, \quad (1)$$

where $I(x, y; \epsilon)$ is the observed image at photon energy ϵ. Then, the reconstructed X-ray image $I(x, y; \epsilon)$ is the inverse Fourier transformation of measured X-ray visibilities $V(u, v; \epsilon)$. Each of the nine *RHESSI* RMCs measures $V(u, v; \epsilon)$ at a fixed spatial frequency (or a circle in the (u, v) plane) corresponding to its angular resolution and with a position angle along the circles, which varies continuously as the spacecraft rotates. Nine detector grids with angular resolutions growing with detector number are logarithmically spaced in the (u, v) plane. Since the measured visibilities sparsely populate the (u, v) plane and have statistical uncertainties, the direct inverse Fourier transform is impractical (Hurford et al. 2002; Schmahl et al. 2007; Massone et al. 2009) and alternative methods should be used.

Assuming a characteristic shape of the X-ray source, one can directly find the position and characteristic sizes by fitting a 2D Fourier image of the model to the *RHESSI* visibilities. Here, we assume that the sources can be presented as elliptical Gaussian sources:

$$I(x, y; \epsilon) = \frac{I_0(\epsilon)}{2\pi\sigma_x\sigma_y} \exp\left(-\frac{(x - x_0(\epsilon))^2}{2\sigma_x^2} - \frac{(y - y_0(\epsilon))^2}{2\sigma_y^2}\right), \quad (2)$$

where $2\sqrt{2\ln 2}\sigma_x$ and $2\sqrt{2\ln 2}\sigma_y$ are FWHMs of an elliptical Gaussian source in the x- and y-direction, respectively, $x_0(\epsilon)$ and $y_0(\epsilon)$ give the position of the source, and I_0 is the total photon flux of the source. One major advantage of the visibility forward fit approach is that, knowing the errors on visibilities $V(u, v; \epsilon)$, one can readily propagate the errors to forward fit parameters of the model in Equation (2). Reliable error estimates for images reconstructed with other algorithms are currently unavailable.

2.1. The Shape of Footpoints for a Limb Event

Using HXR data from *RHESSI*, we analyzed a limb event on 2004 January 6 (*GOES* M5.8 class). As shown previously by Kontar et al. (2008), this event is ideally suited for our analysis, having two well-separated footpoints: one bright and the other much weaker. In addition, the location of the flare at the limb greatly reduces albedo flux (Bai & Ramaty 1978; Kontar et al. 2006) so that the albedo correction (Kontar et al. 2006) becomes negligible.

The flare occurred at the eastern limb near (−975″,75″) from the disk center at ∼06:22 UT (Figure 1). It was imaged during the time of peak emission >50 keV, 06:22:20–06:23:00 UT (indicated by the vertical dotted lines in Figure 1), using

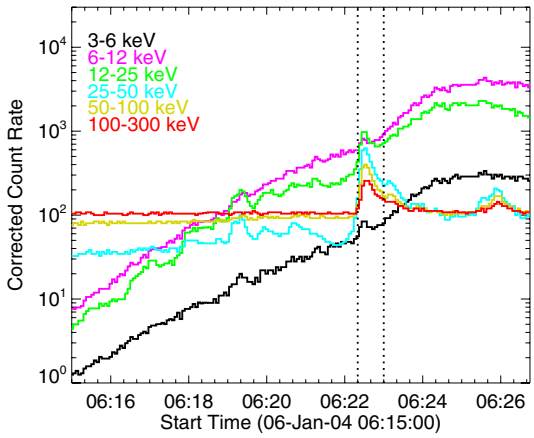

Figure 1. Light curves of the 2004 Jan 6 flare. The vertical dotted lines show the accumulation time interval 06:22:20–06:23:00 UT which is used in the subsequent spectral and imaging analysis.

(A color version of this figure is available in the online journal.)

four different image algorithms (see Figure 2): Clean (Hurford et al. 2002), MEM NJIT (Schmahl et al. 2007), PIXON (Pina & Puetter 1993; Metcalf et al. 1996), and visibility forward fit (Hurford et al. 2002; Schmahl et al. 2007). The resulting images in five energy bands covering the nonthermal emission are shown in Figure 2. Each image was made using the front segments of detectors 2 through 7. Grid 1 with the highest spatial resolution had no significant signal and grids 8–9 are too coarse for our flaring region. Previously, the flare was imaged using 10 energy bins (Kontar et al. 2008) and simple circular Gaussian fit but this was reduced to five wider bins in this paper to improve the signal-to-noise ratio. Figures 2 and 3 demonstrate that the brighter source has an elliptical shape at various energies, so the elliptical Gaussian could be used as natural X-ray distribution model (Figure 3).

Comparing the different algorithm results, we find that CLEANed images have systematically larger sizes than the other algorithms. This is related to the fact that CLEAN images are determined by the user choices for analysis (clean beam size) and not the requirements of the data, and hence should be used with great care to measure source sizes.[1] MEM NJIT has produced smaller source sizes, which could be due to the tendency of the algorithm to over-resolve sources (Schmahl et al. 2007). PIXON (Pina & Puetter 1993; Metcalf et al. 1995) gave us source sizes similar to those of X-ray visibility forward fit. Dennis & Pernak (2009) have also analyzed this event and confirmed the finding of Kontar et al. (2008). We choose to forward fit a circular Gaussian source for the northern footpoint and elliptical Gaussian source (Equation (2)) for the southern footpoint to the visibilities (Equation (1)); the image shown is a reconstruction of the fit results. These fits are shown in Figure 3 and will be discussed in detail in Section 2.2. Assuming two elliptical sources, the weaker source's forward fit parameters have rather large error bars, suggesting that the northern footpoint is not sufficiently well-constrained by the data to be fitted as an elliptical source. In addition, at the energies above 40 keV the weak source is indistinguishable from circular.

[1] Reduction of clean beam size by 1.7 produces images with spatial characteristics similar to other algorithms. Current version of clean does not have robust procedure to determine CLEAN beam size. Note that this correction is only applicable for this particular event and cannot be used universally.

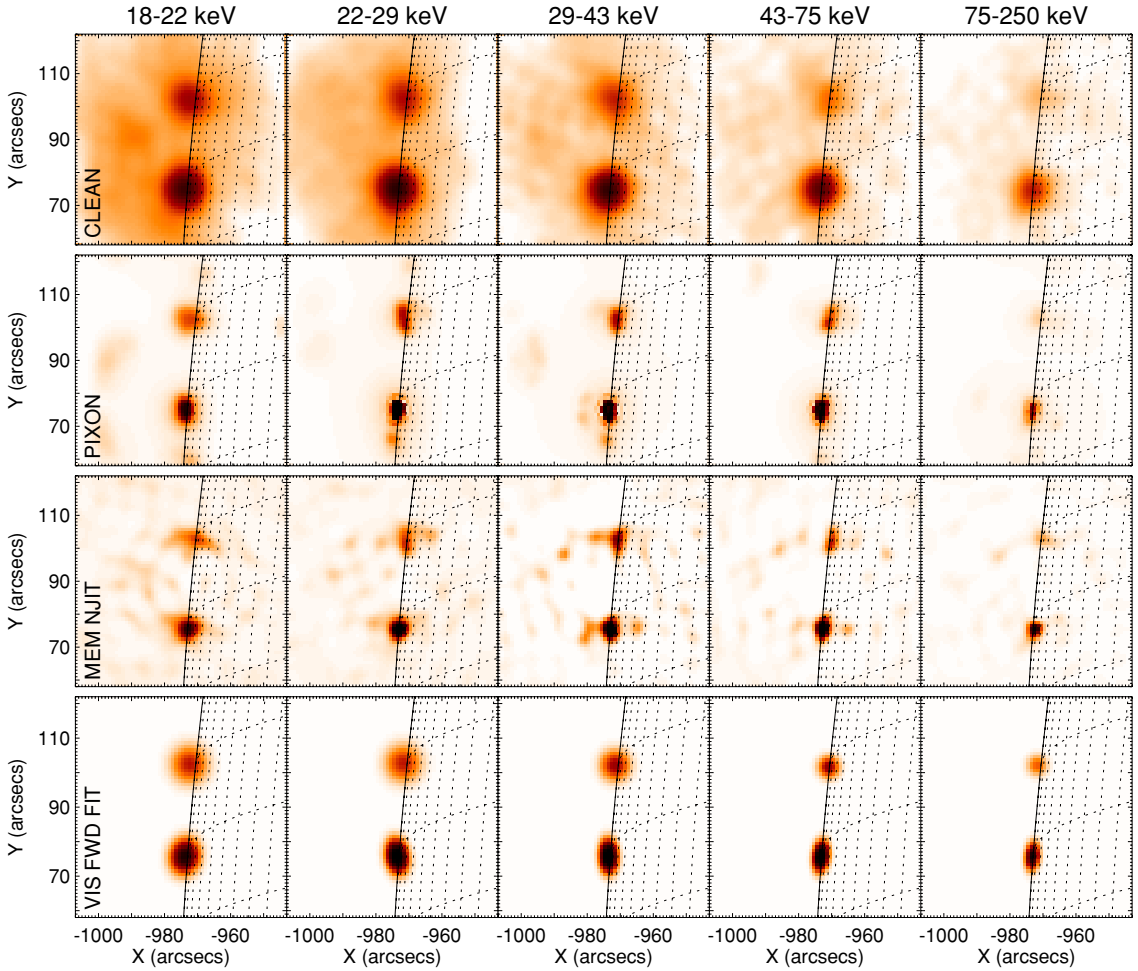

Figure 2. HXR images of the 2004 January 6 flare (accumulation time interval 06:22:20-06:23:00 UT) in five energy ranges: 18–25, 25–29, 29–43, 43–75, and 75–250 keV (energy grows from left to right) using different algorithms: (from top row to bottom) CLEAN, PIXON, MEM-NJIT, and VIS forward fit. Image sizes are 64 × 64 with a pixel size of 1″× 1″. Visibility forward fit images shown here were done using one elliptical (strong southern footpoint) and circular (weak northern footpoint) Gaussian.

(A color version of this figure is available in the online journal.)

The comparison of the images and visibility fit results in Figure 2 shows that the visibility forward fit gives images similar to the ones inferred in other algorithms, although there are differences as pointed out above. Despite the differences between the algorithms, all image reconstruction algorithms show that (1) the southern footpoint has a clear elliptical shape, (2) the shape of the source becomes more elliptical with growing energy, and (3) the size of the source decreases with energy. The northern footpoint is also getting smaller with energy, similar to the southern footpoint (Kontar et al. 2008; Dennis & Pernak 2009), but due to a lower count rate in the source we cannot reliably measure the shape of this source. In addition, since the northern source is not seen above ∼100 keV, it could be partially occulted or have a stronger magnetic convergence (Schmahl et al. 2006) with the energetic electrons precipitating less to dense layers of the chromosphere, producing a fainter footpoint.

2.2. Characteristic Sizes and Footpoint Locations

We focus on the brighter southern footpoint fitted with an elliptical Gaussian (Equation (2)) as more spatial information can be accurately recovered as compared with the northern footpoint. This is a more realistic interpretation of the footpoint shape (see Figure 2) compared with the previously used circular fit (Aschwanden et al. 2002; Kontar et al. 2008).

Each forward fit to X-ray visibilities using an elliptical Gaussian produces six parameters given by Equation (2): positions $x_0(\epsilon)$ and $y_0(\epsilon)$ of the X-ray flux maximum (often called centroid position), FWHM(ϵ), eccentricity $e(\epsilon)$, and position angle $\theta(\epsilon)$, along with error values for each of the parameters. $x_0(\epsilon)$ and $y_0(\epsilon)$ are measured from the disk center and the position angle $\theta(\epsilon)$ is the angle between the north–south line and the semi-major axis of the ellipse. Multiple sources are fitted simultaneously and we fit the weaker northern source with a circular Gaussian. Both sources can be fitted with elliptical sources, producing similar results for the southern footpoint but highly inaccurate results for the northern footpoint. The visibility amplitudes and fits as a function of RMC and spacecraft roll angle are shown in Figure 3. We used between 6 (course grids) and 12 (fine grids) visibilities (spatial Fourier components; Figure 3). The single circular Gaussian fit shows the largest amplitudes of normalized residuals. Two circular Gaussian fits show smaller amplitudes, but larger than the fit using an elliptical plus circular Gaussian fit. The circular plus elliptical fit adequately reproduces the measured photon flux for various roll bins and collimators. We note that at the lowest energies of 18–22 keV, both circular and elliptical plus circular Gaussians give almost identical results. Indeed, both footpoints at 18–22 keV look symmetrical (Figure 2). The

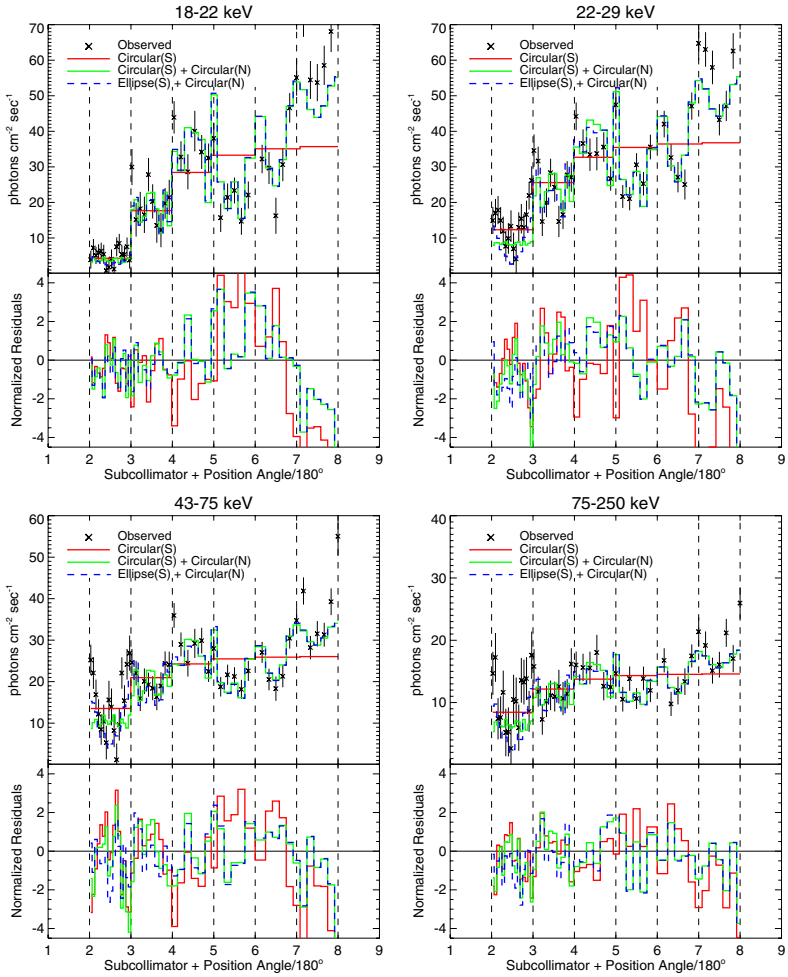

Figure 3. Observed X-ray visibility amplitudes (crosses with error bars) as a function of subcollimator (2–7) and position angle between 0° and 180° of the grids in the stated energy range. The red line shows the fitted model using single circular source, the green line shows two circular Gaussian fits, and the blue dashed line shows an elliptical (southern footpoint) and circular (northern footpoint) Gaussian. The bottom panels show normalized residuals for the corresponding fits.

(A color version of this figure is available in the online journal.)

largest deviations of the fits from the data are found in the coarsest grid and at the lowest energy (Figure 3), which could be caused by the large scale source ($\gtrsim 36''$), which is probably softer X-ray emission from the loop.

Using the $x_0(\epsilon)$, $y_0(\epsilon)$ "centroid positions" of the source for each energy range, the radial height of the source from the solar center can be readily determined for every energy using

$$R(\epsilon) = \sqrt{x_0(\epsilon)^2 + y_0(\epsilon)^2}. \quad (3)$$

The semi-major and semi-minor axes of our elliptical Gaussian fit, $a(\epsilon)$ and $b(\epsilon)$, respectively, are related to the FWHM,

$$\mathrm{FWHM}(\epsilon) = \sqrt{a(\epsilon)b(\epsilon)}, \quad (4)$$

and to the eccentricity,

$$e(\epsilon) = \sqrt{1 - b(\epsilon)^2/a(\epsilon)^2}. \quad (5)$$

Equations (4) and (5) can be solved to find

$$a(\epsilon) = \mathrm{FWHM}(\epsilon)(1 - e(\epsilon))^{-1/4},$$
$$b(\epsilon) = \mathrm{FWHM}(\epsilon)(1 - e(\epsilon))^{1/4}. \quad (6)$$

As the analyzed flare is directly on the eastern limb and close to the solar equator, $a(\epsilon)$ and $b(\epsilon)$ correspond to the source sizes parallel (width) and perpendicular (vertical extent) to the solar surface. The results of the X-ray visibility forward fit parameters are summarized in Figure 4. They again show the trend seen in the images (Figure 2) of decreasing height and source size with energy. We can also see that the source becomes more elliptical at higher energies, starting with $e \sim 0.5$ for 18–22 keV but increasing to $e \sim 0.85$ for 75–250 keV. The circular Gaussian source fitted to the northern footpoint also shows the general trend of decreasing source height and FWHM at higher energies but with considerably larger errors due to this source being weaker.

2.3. Height of X-ray Sources Above the Photosphere

Let us consider the evolution of the electron flux spectrum in the chromosphere $F(E, s)$ along magnetic field lines s using purely collisional transport and ignoring collective effects and effects connected with the magnetic mirroring (Brown et al. 2002). In this approximation, the electron flux spectrum can be written as (Brown 1971)

$$F(E, s) = F_0(E_0)\frac{E}{E_0}, \quad (7)$$

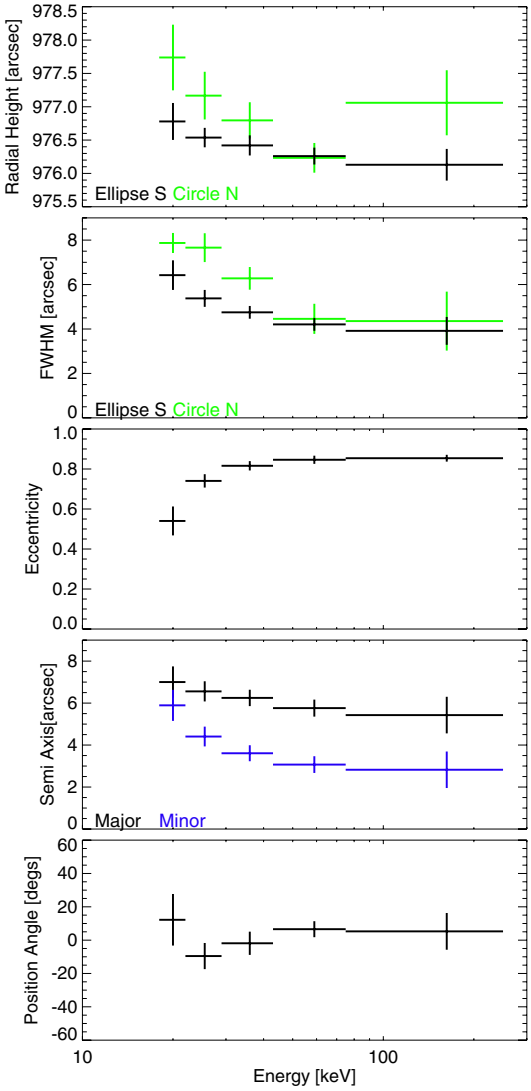

Figure 4. X-ray visibility forward fit parameters as a function of energy: radial distance of the sources, FWHM of the sources, eccentricity, semi-minor and semi-major axes for the northern footpoint, and position angle (the angle between semi-major axis and north–south direction).

(A color version of this figure is available in the online journal.)

where $F_0(E)$ is the injected spectrum of energetic electrons, taken to be a power law of $F_0(E) \propto E^{-\delta}$ and

$$E_0(E,s)^2 = E^2 + 2K\int_0^s n(s')ds', \tag{8}$$

where $K = 2\pi e^2 \ln\Lambda$, $\ln\Lambda$ is the Coulomb logarithm, and e is the electron charge. The chromosphere can be conveniently assumed to be neutral (Brown 1973; Kontar et al. 2002), therefore $\ln\Lambda = \ln\Lambda_{eH} = 7$ (e.g., Brown 1973; Emslie 1978).

The X-ray flux spectrum emitted by the energetic electrons in a magnetic flux tube of cross-sectional area A and observed at 1 AU is given as

$$I(\epsilon,s) = \frac{1}{4\pi R^2} An(s)\int_\epsilon^\infty F(E,s)\sigma(E,\epsilon)dE, \tag{9}$$

where $\sigma(E,\epsilon)$ is the isotropic bremsstrahlung cross section, R is the Sun–Earth distance, and A is the cross-sectional area of the loop. The X-ray flux spectrum expressed by Equation (9)

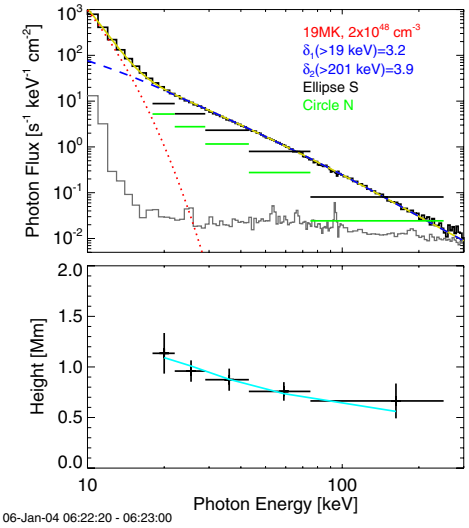

Figure 5. Upper panel: X-ray spectrum of 2004 January 6 flare (solid black histogram) for the accumulation time 06:22:20–06:23:00 UT (see Figure 1) and forward fitted spectrum (yellow line). The photon spectrum was fitted using a thermal (red dotted line) plus thick-target model (blue dashed line). The gray histogram shows the background level. Horizontal black and green lines show the photon flux spectrum from the southern and northern footpoints as found in X-ray visibility forward fits (Figure 2), respectively. The lower panel indicates the results of the forward fit of the source height with collisional model. The fit results are $R_0 = 975\farcs2$ and $h_0 = 155$ km.

(A color version of this figure is available in the online journal.)

has a maximum or an equivalent $dI(\epsilon,s)/ds = 0$ for every energy ϵ because of the growing density along electron path and simultaneously decreasing electron flux due to collisions (Brown et al. 2002; Aschwanden et al. 2002).

Assuming a hydrostatic density profile of

$$n(h = r - r_0) = n_0 \exp\left(\frac{-(r-r_0)}{h_0}\right), \tag{10}$$

where r is the radial distance from the Sun center, the photospheric density $n_0 = 1.16 \times 10^{17}$ cm^{-3} (fixed value; Vernazza et al. 1981), and r_0 is the reference height, we can find these two free parameters h_0 and $r = r_0$ by forward fitting the measured radial distance of the maxima (Figure 5, bottom panel) to the model predicted maxima by the derivative of Equation (9). The height of the sources can be found by subtracting the reference height, r_0, from the radial measurements:

$$h(\epsilon) = r(\epsilon) - r_0. \tag{11}$$

To calculate the reference height, we assumed the density at the photospheric level to be known (Vernazza et al. 1981). This helps to remove substantial uncertainties related to the reference height of the previous studies (cf. Aschwanden et al. 2002; Liu et al. 2006; Mrozek 2006).

We find a spectral index of $\delta = 3.2$ from the spatially integrated spectrum, shown in the top panel of Figure 5. Forward fitting using a hydrostatic density profile gives density scale height of $h_0 = 155 \pm 30$ km and reference height $r_0 = 975\farcs2 \pm 0\farcs2$. From only fitting a circular Gaussian to the southern footpoint, instead of elliptical to southern with circular to the northern as done in this paper, it was previously found that $h = 140 \pm 30$ km and $r_0 = 975\farcs3 \pm 0\farcs2$ (Kontar et al. 2008).

2.4. Vertical Extent of the Footpoint

The characteristic size of the source in the vertical direction (semi-minor axis in our fit) can be straightforwardly estimated

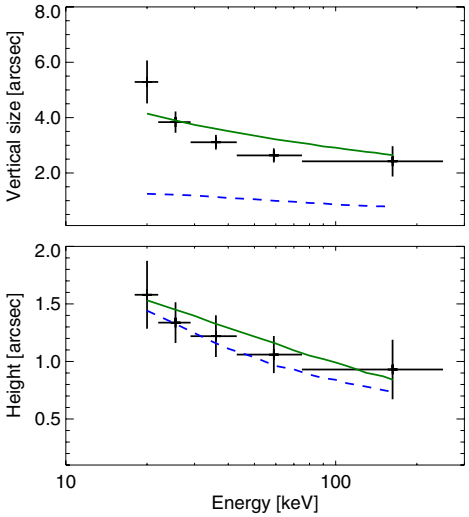

Figure 6. Top panel: FWHM vertical size of the footpoint source (black crosses) as a function of energy, FWHM size given by the thick-target model (Equation (9); blue dashed lines) and multi-thread chromosphere (green lines). Bottom panel: height of the maximum X-ray emission (black crosses) vs. energy.

(A color version of this figure is available in the online journal.)

using the collisional think-target model (Brown 1971) to find the FWHM size from Equation (9) using the density profile found in the previous section. Comparing the measured vertical FWHM size and the prediction of the length from the thick-target model, we see that the measured extent is around 3″–6″ and is 3–6 times larger than the theoretical width (Figure 6). The discrepancy is substantial and cannot be explained in terms of the assumed X-ray source model or error bars.

There are a few plausible explanations that can be given for the observed vertical FWHM size. One is that the structure of the chromosphere may not be uniform over the footpoint cross section and the footpoint is the ensemble of many thin threads (Figure 7) as often seen in high resolution optical images (Lin et al. 2005; De Pontieu et al. 2007; Berkebile-Stoiser et al. 2009). Moreover, it is likely that the deposition of electron energy can lead to upward heating of the chromosphere with the resulting expansion changing the density structure (e.g., Liu et al. 2009).

Let us consider a simple chromospheric model in which the hydrostatic density scale height, h_T, is determined by the temperature of the chromosphere $h_T = k_b T/(\mu m_p g)$, where T is the temperature, k_b is the Boltzmann's constant, m_p is the proton mass, $\mu \simeq 1.27$ is the mean molecular weight (e.g., Aschwanden et al. 2002), and $g \simeq 2.74 \times 10^4$ cm s^{-2} is the solar gravitational acceleration. Thus, the measured density scale height of ∼155 km implies the chromospheric temperature of ∼6500 K. However, the solar atmosphere is not a uniform media but instead is manifested in thin threads (<0.3″) of filaments (Lin et al. 2005), sub-arcsecond dynamic fibrils (De Pontieu et al. 2007), and fine structures of microflares (Berkebile-Stoiser et al. 2009) in the chromosphere with different density profiles in each thread (Figure 7). Following the multi-thread model for the magnetic loop in the chromosphere, we assume that the energetic electrons propagate along different threads with varying density profiles and temperatures in the range from 2200 K up to 20,000 K, corresponding to the density scale heights between ∼50 km and ∼500 km. The average HXR flux from many thin threads will be the measured X-ray distribution. Averaging X-ray emission from a hundred thin threads with temperatures drawn randomly from the above

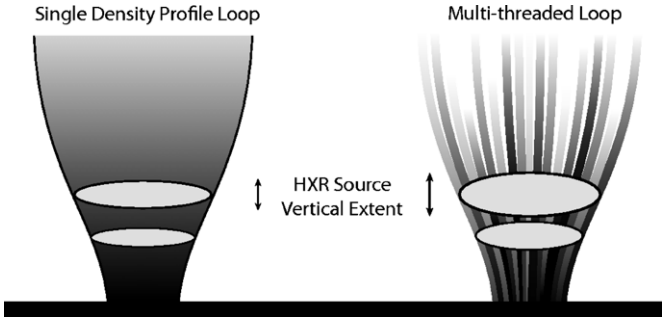

Figure 7. Cross-sectionally uniform (left) and multi-threaded (right) chromospheres. The multi-thread chromosphere leads to the larger vertical sizes of X-ray sources as observed by *RHESSI*.

range, we successfully reproduce the observed vertical sizes (Figure 6).

3. DISCUSSION AND CONCLUSIONS

Using X-ray visibility forward fits, we inferred not only the characteristic sizes and positions but the shapes of HXR sources. The 2004 January 6 event indicates an overall decrease in size of the source and increase of the source ellipticity with energy. The FWHM of the southern source decreases from ∼6.″5 down to around ∼4″ while the ellipticity of the source grows from 0.5 up to 0.9. The source is elongated along the limb as evident in the nearly zero angle between the semi-major axis and the limb; such orientation of the source is observed for all energy ranges. The vertical extent of the source is decreasing by a larger fraction (from 6″ down to 3″) than the horizontal size (from 7″ down to 5.″5) leading to larger elongation of the source along the limb. Hence, the FWHM of the magnetic flux tube containing energetic electrons (semi-major axis) changes from ∼9.7 Mm at height ∼1.1 Mm down to ∼7.6 Mm at 0.6 Mm above the photosphere. The northern footpoint is fainter but shows a similar trend: the higher energies appear at low heights and the size of the source is decreasing with energy suggesting convergence of the magnetic field lines along which electrons propagate. Using X-ray visibilities, we also re-analyzed a flare that occurred on 2002 February 20 that was previously studied by forward fitting time-modulated light curves (Aschwanden et al. 2002). Although this flare is rather weak, we found similar results: the higher energy sources appear at lower heights. The uncertainties are larger than in the 2004 January 6 event but the density model proposed by Aschwanden et al. (2002) is within our error bars. We also note that the size of the sources in the February 20 flare decreases with energy, similar to the event on January 6.

Analyzing HXR emission from footpoints, we found that various imaging algorithms (PIXON, Visibility Forward Fit, CLEAN, MEM-NJIT, etc.) give generally similar results for spatial distributions of X-ray footpoints. Although *RHESSI* imaging algorithms can be adjusted by the parameter choice and hence X-ray images could be somewhat altered, there is a general trend for the algorithms. CLEAN, with its default set of parameters, has a tendency to provide larger sources, while MEM-NJIT tends to over-resolve X-ray sources. PIXON and visibility forward fit show very similar results. Visibility forward fit allows us to study the sub-arcsecond distribution of HXR sources in suitably orientated bright flares. Due to systematic differences in sizes we obtained for 2004 January and 2002 February flares, we suggest that, for source size/shape measurements of X-ray sources, CLEAN and MEM-NJIT should be used with extreme caution.

The northern footpoint could be partially occulted as the highest energy photons come predominantly from the southern footpoint, but we note that this bright footpoint is unlikely to be occulted. As pointed out by G. Hurford,[2] a source partially subtended by the solar disk should have a sharp edge, where the brightness of the source will drop from maximum to zero over rather small radial distance. The derivative of the source brightness in the x-direction (perpendicular to the limb), $\partial I(x, y)/\partial x$, will have a maximum at the limb, where $I(x, y)$ has the sharp drop. It is evident from Equation (1) that the corresponding visibilities, $2\pi i u V(u, v)$, should have a well pronounced maximum, which should be evident in the measured amplitudes of visibilities. Specifically, the finer grid RMCs should show large amplitudes when the grids are parallel to the limb, i.e., the visibility amplitudes are much larger at the phase angles 0° and 180°, which is not evident in the event under study (cf. Figure 3). To make the discussion more complete, we note that the line-of-sight effects cannot be definitively ruled out. The footpoints might be projections of two rather long flare ribbons viewed almost parallel to the line of sight, so that the vertical extension is the projection of a different height. Finally, we should note that if the occultation height is small, $\lesssim 0\farcs5$, our height measurements are lower limits, but the major conclusion about the vertical extent is the same. If, though unlikely, the lower part of the loop (footpoints) is occulted, these observations provide an interesting question to the flare models as to why the sources' sizes decrease with energy, and the higher energy sources appear lower and not at the lowest visible location where the density is the highest.

Our measurements show that while the locations of the maxima of X-ray emission are consistent with simple collisional transport in a single density scale height chromosphere, the vertical sizes do not agree with the assumption of field aligned electron transport. The vertical extent of X-ray sources is 3–6 times larger than in the purely collisional model in a single density scale height chromosphere. However, a chromospheric model involving multiple density threads within the flux tube of a footpoint can explain both the position of the maximum and the vertical size of the sources. We note that pitch angle scattering due to Coulomb collisions is likely to be insufficient to produce such a strong expansion. The X-ray source size increase due to collisional pitch angle scattering will be about a quarter of the electron stopping depth for initially field aligned electrons (Conway 2000). However, strong non-collisional scattering or wave–particle interactions (e.g., Hannah et al. 2009) might boost the vertical source sizes to the measured value and hence cannot be excluded, and will also be consistent with the lack of downward anisotropy found in X-ray flare emission (Kontar & Brown 2006; Kasparová et al. 2007). We note that the adopted model does not account for the magnetic field and its effects on particle transport, which could lead to larger source sizes and is a subject of additional modeling.

The authors are thankful to Gordon Hurford for insightful suggestions and Richard Schwartz for referee comments. This work was supported by a STFC rolling grant (I.G.H. and E.P.K.), STFC/PPARC Advanced Fellowship (E.P.K.), and the Leverhulme Trust (M.B. and E.P.K.). Financial support by the European Commission through the SOLAIRE Network (MTRN-CT-2006-035484) is gratefully acknowledged. The work has benefited from ISSI, Bern visitor programme.

REFERENCES

Aschwanden, M. J., Brown, J. C., & Kontar, E. P. 2002, Sol. Phys., 210, 383
Bai, T., & Ramaty, R. 1978, ApJ, 219, 705
Battaglia, M., & Benz, A. O. 2007, A&A, 466, 713
Berkebile-Stoiser, S., Gömöry, P., Veronig, A. M., Rybák, J., & Sütterlin, P. 2009, A&A, 505, 811
Brown, J. C. 1971, Sol. Phys., 18, 489
Brown, J. C. 1973, Sol. Phys., 28, 151
Brown, J. C., Aschwanden, M. J., & Kontar, E. P. 2002, Sol. Phys., 210, 373
Conway, A. J. 2000, A&A, 362, 383
De Pontieu, B., Hansteen, V. H., Rouppe van der Voort, L., van Noort, M., & Carlsson, M. 2007, ApJ, 655, 624
Dennis, B. R., & Pernak, R. L. 2009, ApJ, 698, 2131
Emslie, A. G. 1978, ApJ, 224, 241
Emslie, A. G., Kontar, E. P., Krucker, S., & Lin, R. P. 2003, ApJ, 595, L107
Fivian, M. D., Krucker, S., & Lin, R. P. 2009, ApJ, 698, L6
Hannah, I. G., Kontar, E. P., & Sirenko, O. K. 2009, ApJ, 707, L45
Hurford, G. J., et al. 2002, Sol. Phys., 210, 61
Kašparová, J., Kontar, E. P., & Brown, J. C. 2007, A&A, 466, 705
Kontar, E. P., & Brown, J. C. 2006, ApJ, 653, L149
Kontar, E. P., Brown, J. C., & McArthur, G. K. 2002, Sol. Phys., 210, 419
Kontar, E. P., Hannah, I. G., & MacKinnon, A. L. 2008, A&A, 489, L57
Kontar, E. P., MacKinnon, A. L., Schwartz, R. A., & Brown, J. C. 2006, A&A, 446, 1157
Kosugi, T., et al. 1992, PASJ, 44, L45
Krucker, S., & Lin, R. P. 2008, ApJ, 673, 1181
Lin, R. P., et al. 2002, Sol. Phys., 210, 3
Lin, Y., Engvold, O., Rouppe van der Voort, L., Wiik, J. E., & Berger, T. E. 2005, Sol. Phys., 226, 239
Liu, W., Liu, S., Jiang, Y. W., & Petrosian, V. 2006, ApJ, 649, 1124
Liu, W., Petrosian, V., & Mariska, J. T. 2009, ApJ, 702, 1553
Massone, A. M., Emslie, A. G., Hurford, G. J., Prato, M., Kontar, E. P., & Piana, M. 2009, ApJ, 703, 2004
Matsushita, K., Masuda, S., Kosugi, T., Inda, M., & Yaji, K. 1992, PASJ, 44, L89
Metcalf, T. R., Hudson, H. S., Kosugi, T., Puetter, R. C., & Pina, R. K. 1996, ApJ, 466, 585
Metcalf, T. R., Jiao, L., McClymont, A. N., Canfield, R. C., & Uitenbroek, H. 1995, ApJ, 439, 474
Mrozek, T. 2006, Adv. Space Res., 38, 962
Piana, M., Massone, A. M., Hurford, G. J., Prato, M., Emslie, A. G., Kontar, E. P., & Schwartz, R. A. 2007, ApJ, 665, 846
Pina, R. K., & Puetter, R. C. 1993, PASP, 105, 630
Prato, M., Emslie, A. G., Kontar, E. P., Massone, A. M., & Piana, M. 2009, ApJ, 706, 917
Saint-Hilaire, P., Krucker, S., & Lin, R. P. 2008, Sol. Phys., 250, 53
Schmahl, E. J., Pernak, R., & Hurford, G. 2006, BAAS, 38, 241
Schmahl, E. J., Pernak, R. L., Hurford, G. J., Lee, J., & Bong, S. 2007, Sol. Phys., 240, 241
Vernazza, J. E., Avrett, E. H., & Loeser, R. 1981, ApJS, 45, 635
Xu, Y., Emslie, A. G., & Hurford, G. J. 2008, ApJ, 673, 576

[2] Presentation at 9th *RHESSI* workshop in Genoa: http://sprg.ssl.berkeley.edu/~krucker/genoa/position/XrayLimb-Genoa.ppt.